infrastructures

Article

Optimal Monitoring Section Layout for iFEM-Based Strain Reconstruction of Subsea Pipelines via Greedy Search

Xueyu Ren [1], Jiawang Chen [2,*], Shang Sun [1], Jianling Zhou [1], Zhonghui Zhou [2] and Yuan Lin [1]

1 Ocean College, Zhejiang University, Zhoushan 316000, China; 12234022@zju.edu.cn (X.R.); shang_sun@zju.edu.cn (S.S.); 13454099962@163.com (J.Z.); samylin@zju.edu.cn (Y.L.)
2 Donghai Laboratory, Zhoushan 316000, China; zzhok@163.com
* Correspondence: arwang@zju.edu.cn

Abstract

Subsea oil and gas pipelines are critical infrastructure in marine engineering, and strain monitoring is essential for their safe operation. However, due to the complexity of the marine environment and the constraints practical deployment, engineering applications often rely on sparse monitoring points, making it difficult to directly obtain full-field strain information. To address this issue, this paper proposes a strain field reconstruction method for subsea suspended pipelines based on the inverse finite element method (iFEM) and a greedy search strategy, and provides the corresponding optimal layout of monitoring cross-sections. Using a constructed numerical simulation library under multiple load cases, algorithm validation and parameter calibration are performed. On this basis, a comprehensive evaluation framework incorporating both global and peak errors is established. Results show that under the greedy-optimized monitoring section scheme, the comprehensive reconstruction error of iFEM ranges from 0.030 to 0.035, the axial strain error is significantly lower than the circumferential strain error, and the peak relative error stabilizes when the number of monitoring sections reaches seven. The proposed method overcomes the difficulty of acquiring full-field strain information under sparse monitoring conditions, and can provide technical support for the structural health monitoring and safety assessment of subsea oil and gas pipelines.

Keywords: subsea suspended pipeline; inverse finite element method (iFEM); greedy search; monitoring-section optimization; full-field strain reconstruction

Check for updates

Academic Editors: Zifeng Zhao and Jin Li

Received: 6 April 2026
Revised: 29 April 2026
Accepted: 30 April 2026
Published: 6 May 2026

1. Introduction

Subsea oil and gas pipelines are key infrastructure in the marine energy transmission system, and their long-term safe operation has high requirements in terms of structural integrity monitoring and evaluation [1–3]. Under the combined action of environmental loads such as waves and ocean currents, the suspended span section of the pipeline is prone to significant bending deformation and strain concentration, making it an area with a high risk of fatigue damage and failure [4]. In order to continuously understand the operating status of pipelines, Structural Health Monitoring (SHM) technology has been gradually applied to the safety assessment and operation management of subsea pipelines [5,6]. Conventional methods based on pressure and flow data (e.g., Pérez-Pérez et al. [7,8]) have been developed for leak detection, but they cannot provide distributed strain information. Recently, distributed optical fiber sensor (DOFS) technology has emerged as a promising alternative for pipeline monitoring. For instance, Liang et al. [9]. used a dual-parameter

 https://doi.org/10.3390/infrastructures11050160

fiber optic system (Raman temperature + Rayleigh vibration) to achieve leak identification with 92.16% accuracy and 1 m localization; Lalam et al. [10]. developed a multi-parameter DOFS capable of monitoring strain, temperature, vibration, and chemical changes over 25 km. DOFS technology has gained popularity in pipeline monitoring owing to its minimal footprint, corrosion resistance, and anti-electromagnetic interference [11–13]. However, due to factors such as the complex underwater environment, difficulties in sensor deployment, and high maintenance costs, how to reliably evaluate the overall condition of the structure based on limited monitoring information has become one of the key issues in structural health monitoring research [14,15].

In recent years, online or quasi-online condition assessment of subsea suspended span pipelines has gradually become an important research topic in the health monitoring of marine engineering structures [16–19]. However, due to the complex underwater environment and cost factors, the scale of sensor deployment is usually greatly limited, and structural state reconstruction and identification under sparse strain monitoring conditions still face great challenges. Especially under the premise of limited monitoring resources, a means of determining the key monitoring section that can take into account reconstruction accuracy and layout efficiency has become one of the core issues in studies on the sparse monitoring of subsea pipelines [16].

Regarding the problem of full-field reconstruction under sparse strain monitoring conditions, existing research has roughly formed two representative technical paths. The first is the data-driven method, represented by the interpolation method, which expands the limited monitoring point information into a continuous strain field to obtain the reconstructed results for the full-field state [20–22]. In 2023, Wang et al. proposed the experimental strain field reconstruction method (EXP-SFRM) based on the idea of interpolation [20]. This method can better restore the overall strain distribution characteristics under limited measuring point conditions and obtain high reconstruction accuracy in experimental tests. However, it should be noted that conventional interpolation methods are prone to large errors when the strain distribution is complex. During the circumferential expansion of cylindrical surface strain data, if there is no periodic constraint, discontinuities or unreal numerical anomalies may easily occur near the periodic boundaries. In response to this problem, in 2024, Dong et al. proposed the Filtered Kriging framework, which improved the ability to reconstruct extreme areas while maintaining field continuity [21]. Another study further enhanced the ability to express local changing features by introducing methods such as radial basis interpolation [22]. Despite these improvements, interpolation methods lack mechanical consistency and struggle to generalize across varying load conditions.

The other type of method is the physical model method, represented by the inverse finite element method. This method achieves consistent reconstruction of the displacement field and strain field under the condition of sparse monitoring points by minimizing the residual error between the reconstructed strain and the monitored strain, combined with structural mechanics constraints [23–26]. In 2024, Wu et al. proposed an improved method based on energy regularization using the traditional inverse finite element method (iFEM) framework for the reconstruction of structural deformation fields and structural health monitoring [23]. This method introduces regularization constraints into the error functional species, thereby improving the solution stability and reliability of results under insufficient monitoring data or in the presence of noise. In 2025, Li et al. proposed an enhanced framework that combines strain pre-extrapolation with iFEM to supplement observation information without increasing the number of monitoring points and improve the quality of full-field reconstruction [24].

In addition to the reconstruction algorithm itself, the layout of sparse monitoring points also directly affects the reconstruction accuracy. Therefore, how to reasonably configure the positions of monitoring points under the constraints of a limited number of monitoring points to increase the accuracy and robustness of full-field reconstruction has also become an important topic in sparse monitoring research [27,28]. In 2022, Ghasemzadeh et al. combined the iFEM with the genetic algorithm (GA) to construct a sensor layout optimization framework for plate and shell structures, and aimed to achieve higher reconstruction accuracy with as few measuring points as possible [27]. In addition, in 2018, Zhao et al. combined eigenvalue analysis and the particle swarm optimization (PSO) algorithm to conduct point layout optimization research [28]. The experimental results verified the accuracy and robustness of iFEM in detecting structural deformation.

At present, research on full-field strain reconstruction and monitoring-section optimization for subsea suspended pipelines under sparse strain monitoring conditions remains limited. Existing studies lack a systematic integration of monitoring layout design, strain field reconstruction, and performance evaluation, and inconsistencies in evaluation criteria are often observed when comparing different methods. More importantly, most existing work focuses primarily on improving reconstruction algorithms while paying insufficient attention to the selection of monitoring sections, which directly affects reconstruction performance. Consequently, a collaborative analytical framework that links monitoring-section optimization with reconstruction performance for different methods has yet to be established.

To address these issues, this paper constructs a numerical simulation case library under multiple loading conditions and introduces a greedy search strategy to optimize the monitoring sections for the iFEM method, thereby obtaining an optimal monitoring-section scheme that aligns with its reconstruction mechanism. This scheme is then used to perform a full-field strain reconstruction for the subsea suspended pipeline. By establishing a comprehensive evaluation framework that includes both global error and peak error, this study quantitatively compares the reconstruction performance of the optimal monitoring-section scheme under different numbers of monitoring sections. This work integrates monitoring-section optimization, full-field strain reconstruction, and a performance evaluation, providing a quantitative basis for monitoring scheme design in the health assessment of subsea suspended pipelines.

The remainder of this paper is structured as follows. Section 2 introduces the mathematical modeling of the iFEM reconstruction framework and its core algorithmic principles. Section 3 describes the numerical simulation setup and parameter configuration, based on which simulated monitoring data are extracted from discrete monitoring points to determine the optimal sparse monitoring point distribution for the iFEM algorithm. Section 4 determines the optimal sparse monitoring-section distribution scheme for the iFEM algorithm using the greedy search strategy, and analyzes the errors in the accuracy of iFEM under different numbers of sections, thereby identifying the optimal monitoring locations and optimal number of sensors under sparse strain monitoring conditions. Section 5 summarizes the main conclusions of this paper and outlines future research directions.

2. Methods

In order to study the full-field strain reconstruction problem of subsea suspended-span pipelines under sparse strain monitoring conditions, this paper aims to restore the continuous strain field on the outer surface of the pipeline and conducts an analysis of field information reconstructions, comparing different methods under limited observation conditions. Considering that the pipeline surface has both axial extension and circumferential closure characteristics, this paper first uses a parametric method to uniformly describe the surface strain distribution and establishes a unified analysis framework suitable for different reconstruction methods.

2.1. Problem Definition and Validation Strategy

This paper aims to address the problem of reconstructing the global strain field of a suspended pipeline using data acquired under sparse strain monitoring conditions. Specifically, it reconstructs a continuous strain field on the outer surface of a pipe cylinder as $\hat{\varepsilon}(x, \theta)$, and the reference strain field obtained by numerical simulation is represented as $\boldsymbol{\varepsilon}^{ref}(x, \theta)$. In order to unify the data organization and visualization of results, this paper first parametrically maps the cylindrical surface to a two-dimensional area, and defines the corresponding reconstruction operator and evaluation process in this parameter domain.

2.1.1. Geometric Parametrization

To accurately characterize the geometric features of the pipe surface and simplify subsequent calculations, this paper adopts a cylindrical coordinate system for parametric description. Specifically, the outer surface of the pipe is parameterized by the axial coordinate x and the circumferential angle θ, and the corresponding two-dimensional parameter domain $\boldsymbol{\Omega}(x,\theta)$ is defined as

$$\Omega = \{(x, \theta) | x \in [-L/2, L/2], \theta \in [0, 2\pi)\} \tag{1}$$

where L denotes the length of the suspended span. Due to the closed nature of the pipe in the circumferential direction, $\theta = 0$ and $\theta = 2\pi$ correspond to the same physical location; therefore, the strain field satisfies a periodic continuity condition along the θ-direction.

2.1.2. Generation of Sparse Monitoring Data Based on Numerical Benchmarks

In order to verify the performance of the reconstruction method, this paper uses the full-field strain obtained by numerical simulation as the numerical benchmark, and extracts the strain value at the corresponding position on the preset sparse measuring point set P:

$$P = \{(x_i, \theta_i)\}_{i=1}^{N} \tag{2}$$

x_i represents the axial coordinate of a monitoring section, and θ_i represents the circumferential angle of a measuring point.

On this basis, a sparse monitoring vector is constructed:

$$\boldsymbol{\varepsilon}^{\text{obs}} = \left[\varepsilon^{\text{ref}}(x_1, \theta_1), \varepsilon^{\text{ref}}(x_2, \theta_2), \ldots, \varepsilon^{\text{ref}}\left(x_{N_p}, \theta_{N_p}\right)\right]^{\top}, \tag{3}$$

where $\varepsilon^{\text{ref}}\ (x, \theta)$ denotes the numerical benchmark full-field strain (reference ground truth), and $\boldsymbol{\varepsilon}^{\text{obs}}$ is the sparse monitoring vector obtained by sampling the reference field at the preset sparse monitoring point set P. During the reconstruction process, the above sparse monitoring vectors are used as input to the algorithm. The reconstruction verification framework and specific evaluation process based on the numerical benchmark field are shown in Figure 1.

2.1.3. Regularized Formulation of the Reconstruction Problem

Strain field reconstruction can be regarded as an inverse mapping problem of restoring continuous field distribution from sparse monitoring information [29]. Define the reconstruction operator $H(\cdot)$; then, the reconstructed strain field $\hat{\varepsilon}(x, \theta)$ is obtained by:

$$\hat{\varepsilon}(x, \theta) = \mathcal{H}\left(\boldsymbol{\varepsilon}^{\text{obs}}; \Omega, K\right) \tag{4}$$

$\boldsymbol{\varepsilon}^{\text{obs}}$ is the sparse monitoring vector, Ω represents the spatial domain or observation point set corresponding to the observation information, and K represents the introduced prior information. In order to obtain a stable solution, this paper further writes the problem into a regularized optimization form:

$$\hat{\varepsilon} = \arg\min_{\varepsilon}\left(\left\|\mathcal{C}(\varepsilon) - \boldsymbol{\varepsilon}^{\text{obs}}\right\|_2^2 + \lambda\|\mathcal{U}(\varepsilon)\|_2^2\right), \tag{5}$$

$C(\cdot)$ is the sampling operator. The first term is used to ensure consistency between the reconstruction results and the monitoring data. $\mathcal{U}(\cdot)$ is the regularization term, which is used to alleviate the ill-posedness of the problem and improve the stability of the numerical solution. λ is the trade-off coefficient.

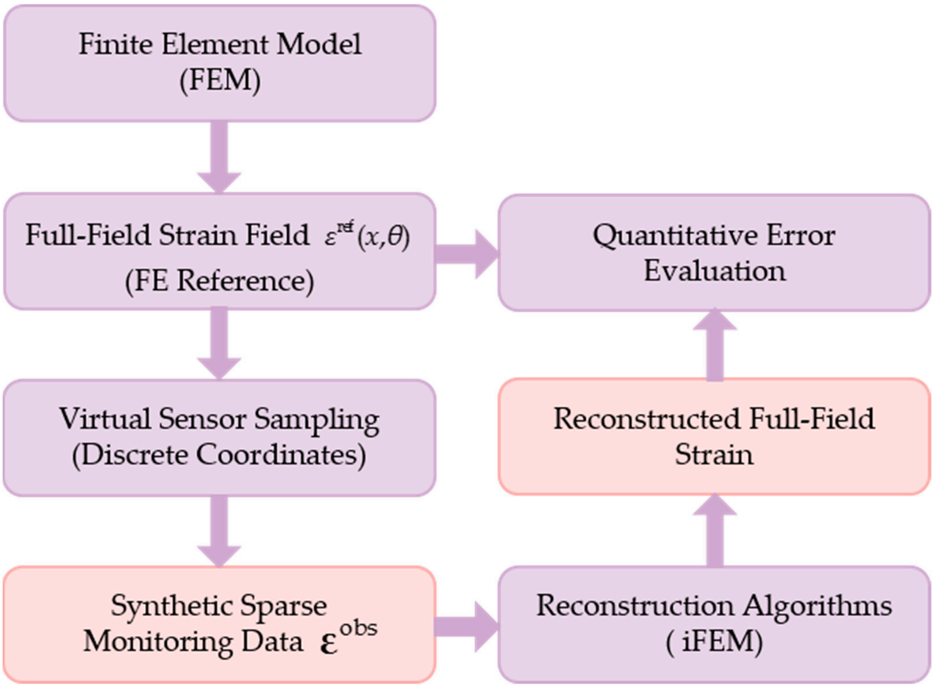

Figure 1. Flowchart for the Numerical Benchmark Verification and Evaluation of Strain Reconstruction for Pipelines.

Under the unified problem formulation presented above, iFEM constructs an objective function through residual terms and regularization terms under a weighted least squares framework, and combines structural kinematic constraints to achieve a physical information-driven inversion reconstruction. The specific methods that were implemented can be found in Section 2.2.

2.2. Strain Field Reconstruction Based on Inverse Shell Finite Elements

iFEM introduces structural kinematic relations and continuity constraints, and by minimizing the weighted residual difference between the reconstructed strain and the reference strain, a strain field that satisfies mechanical consistency can still be obtained, even under sparse measurement conditions. This paper uses the four-node inverse shell element iQS4 based on first-order shear deformation theory (FSDT). Its unit structure and kinematic assumptions can be found in the relevant literature [30].

2.2.1. Mechanical Description of the Inverse Shell Element

Under the FSDT framework, the displacement vector of any point in the unit can be obtained by linear interpolation from the node degrees of freedom:

$$\mathbf{u}(\xi,\eta) = \mathbf{N}(\xi,\eta)\mathbf{d}^e, \tag{6}$$

ξ and η are the natural coordinates of the shell element, and the value range is usually $[-1, 1]$. They are used to define the shape function $\mathbf{N}(\xi, \eta)$ and complete the Gaussian integral calculation. $\mathbf{d}^e$ is the unit node degree of freedom vector; each node contains 6 degrees of freedom and the unit has a total of 24 degrees of freedom. Regarding the definition of degrees of freedom of the iQS4 unit and its geometric relationships, please refer to the literature [30]; this article will not repeat the derivation. Figure 2 shows the degree of freedom distribution and structural characteristics of the iQS4 unit.

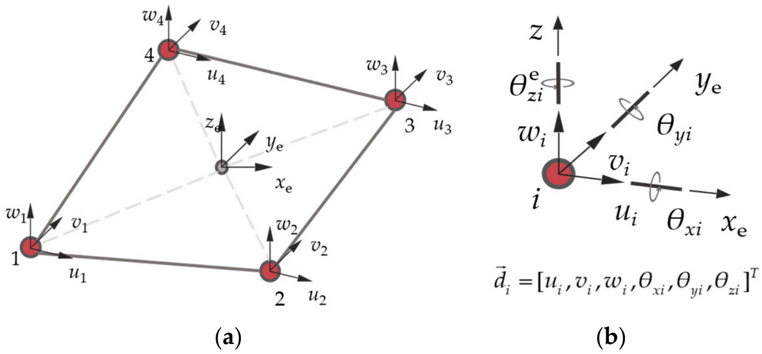

Figure 2. Geometry and nodal degrees of freedom of the inverse shell element: (**a**) element configuration and nodal layout; (**b**) definition of the nodal displacement components in the local coordinate system.

Furthermore, the unit theoretical strain vector can be obtained from the displacement gradient and can be written in a standard linear form:

$$\boldsymbol{\varepsilon}(\xi,\eta) = \mathbf{B}(\xi,\eta)\mathbf{d}^e = \begin{bmatrix} \mathbf{B}^m(\xi,\eta) \\ \mathbf{B}^k(\xi,\eta) \\ \mathbf{B}^s(\xi,\eta) \end{bmatrix} \mathbf{d}^e, \tag{7}$$

where $\boldsymbol{\varepsilon} = \left[\boldsymbol{\varepsilon}^m; \boldsymbol{\varepsilon}^k; \boldsymbol{\varepsilon}^s\right]^\top$ is the strain vector, composed of membrane strains ($\boldsymbol{\varepsilon}^m$) bending curvatures ($\boldsymbol{\varepsilon}^k$), and transverse shear strains ($\boldsymbol{\varepsilon}^s$). The sub-matrices $\mathbf{B}^m$, $\mathbf{B}^k$ and $\mathbf{B}^s$ share the corresponding strain–displacement matrices. Their explicit expressions, derived from the displacement gradients and the shape functions $\mathbf{N}(\xi,\eta)$, can be found in the classic iQS4/iFEM literature [30].

2.2.2. Weighted Least Squares Error Function

In order to balance the role of different observed strain components in the reconstruction process and improve the stability of numerical solutions under sparse monitoring conditions, this paper constructs a weighted least squares error functional, including component-weighted residual terms and regularization terms at the unit level. For unit e, its error functional is defined as

$$\Pi^e(\mathbf{d}^e) = \int_{\Omega^e} \left[w_x \left(\varepsilon_x(\mathbf{d}^e) - \varepsilon_x^{obs} \right)^2 + w_\theta \left(\varepsilon_\theta(\mathbf{d}^e) - \varepsilon_\theta^{obs} \right)^2 \right] \mathrm{d}\Omega + \lambda_s \int_{\Omega^e} \|\nabla w(\mathbf{d}^e)\|^2 \mathrm{d}\Omega + \lambda_{Tik} ||\mathbf{d}^e||_2^2, \tag{8}$$

ε_x^{obs} and ε_θ^{obs} respectively, represent the axial and circumferential monitoring strain components, and w represents the normal displacement components of the mid-shell surface; w_x and w_θ are the weight coefficients of the axial and circumferential strain residual terms, respectively; λ_s is the normal displacement gradient smoothing term coefficient and λ_Tik is the Tikhonov stability term coefficient.

The actual input monitoring components in this article are ε_x^{obs} and ε_θ^{obs}. Although the remaining generalized strain components that are not directly observed do not appear explicitly in the residual term, because they share the same set of displacement degree-of-freedom vectors $\mathbf{d}^e$ as the observed components and are coupled to each other through the shell kinematic relationship, they will still have an indirect constraint effect on the final reconstruction result. The parameter values in Equation (8) are presented in Section 3.3.2.

By finding the extreme value $\prod^e$ of $\mathbf{d}^e$, the linear equation at the unit level can be obtained:

$$\mathbf{K}^e\mathbf{d}^e = \mathbf{F}^e, \tag{9}$$

$\mathbf{K}^e$ and $\mathbf{F}^e$ are obtained by the numerical integration of Equations (6)–(8), representing the iFEM unit coefficient matrix and equivalent load vector respectively. Its specific expansion form and integral implementation process are consistent with the standard implementation of iQS4. This article will not expand each individually. The relevant derivation can be found in the literature [30].

Global assembly is carried out according to the unit topological relationship, and we can obtain:

$$\mathbf{KD} = \mathbf{F}, \tag{10}$$

$\mathbf{K}$ and $\mathbf{F}$ are assembled from units $\mathbf{K}^e$ and $\mathbf{F}^e$ respectively, and $\mathbf{D}$ represents the global degree-of-freedom vectors. In order to suppress the rigid body mode and impose end constraints, this paper uses the penalty function method to introduce boundary conditions in the global equation, as shown in Figure 3, thereby obtaining the modified global equation:

$$(\mathbf{K} + \beta\mathbf{K}_{bc})\mathbf{D} = \mathbf{F} + \beta\mathbf{F}_{bc}, \tag{11}$$

β is the boundary penalty parameter; $\mathbf{K}_{bc}$ and $\mathbf{F}_{bc}$ represent the penalty matrix and penalty vector corresponding to the constraint equation, respectively. After solving this equation, the global degree of freedom vector $\mathbf{D}$ can be obtained, and the strain field can be reconstructed through back-substitution.

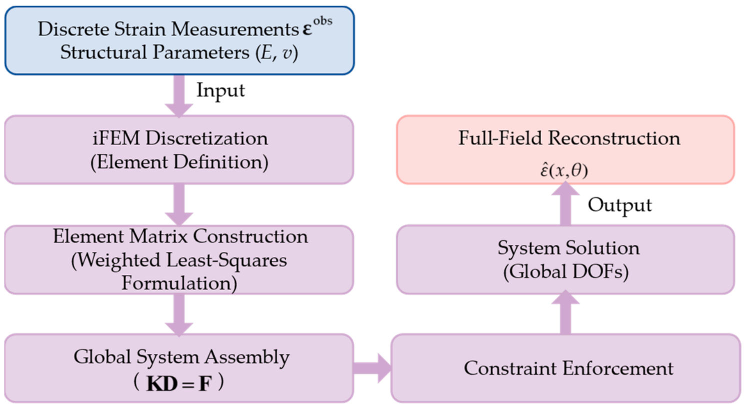

Figure 3. Global Matrix Assembly and Displacement Field Inversion Process based on iFEM.

2.3. Greedy Search Strategy for the Optimization of Monitoring Cross-Sections with Different Algorithms

2.3.1. Unified Feasible Region Constraints

Under a limited monitoring budget, the spatial layout of the monitoring section will directly affect the accuracy and stability of the full-field strain reconstruction. In order to improve the information utilization efficiency under the condition of limited measuring points, this paper introduces a greedy search strategy for monitoring cross-section optimization based on different algorithm characteristics under the constraints of a unified candidate space and a unified feasible region. This strategy aims to minimize the reconstruction error in the training condition set and gradually selects the current optimal

https://doi.org/10.3390/infrastructures11050160

candidate monitoring section, thereby constructing monitoring section schemes that match the reconstruction mechanisms for the interpolation method and iFEM, respectively.

In order to ensure that the two methods can be compared under the same conditions, this paper uses the same set of candidate monitoring sections and consistent feasible region constraints for the interpolation method and iFEM. The difference between the two is only reflected in the reconstruction error feedback mechanism, ensuring the fairness and comparability of the optimization process.

Suppose the set of pipeline axial candidate sections is

$$V = \{x_1, x_2, \ldots, x_B\}, \tag{12}$$

x_m represents the axial position of the m-th candidate monitoring section, and V is the candidate set, composed of all candidate monitoring sections. This paper uses the monitoring section as the basic optimization unit. Each selected monitoring section is equipped with four fixed circumferential measuring points, and the measuring point interval is 90°. This practical choice ensures convenient subsea installation (using the pipeline's horizontal and vertical baselines) and sufficient sampling of low-order circumferential strains for iFEM-based reconstruction. The positions of the measuring points within the section remain fixed and are not used as optimization variables. Therefore, when Ns monitoring sections are selected, the total number of monitoring points is $4N_s = N_p$.

Under a given budget N_s, the monitoring section optimization problem can be expressed as follows: select the optimal section subset S from the candidate set V to minimize the aggregate reconstruction error on the training condition set, that is,

$$\min_{S \subseteq \mathcal{V}} J(S), \quad \text{s.t. } |S| = N_s, \tag{13}$$

$J(S)$ represents the aggregate reconstruction error of the candidate monitoring section subset S on the training condition set.

In order to ensure that the interpolation method and iFEM are compared under the same conditions, this paper uses unified feasible region constraints. Specifically, the candidate interface needs to satisfy the axial range constraints:

$$|x| \leq x_{\text{limit}}, \tag{14}$$

The minimum interface spacing constraints are as follows:

$$|x_i - x_j| \geq d_{\min}, \; x_i, x_j \in S, i \neq j \tag{15}$$

The above constraints jointly limit the feasible search domain of candidate layouts, allowing the two reconstruction methods to be optimized and compared under consistent layout boundary conditions.

2.3.2. Forward Greedy Search Criterion

Under the constraints of a unified candidate space and a unified feasible region, this paper adopts the forward greedy strategy to gradually construct the optimal monitoring cross-section set. Assume that the selected set after the $(k-1)$-th round of iteration is S_{k-1}. For any candidate monitoring section $x \in V \backslash S_{k-1}$ that satisfies the constraints and has not yet been selected, construct a temporary set:

$$S_k^{(x)} = S_{k-1} \cup \{x\}, \tag{16}$$

Subsequently, the corresponding monitoring scheme is generated based on the temporary set, and a complete reconstruction evaluation is performed on the training condition set. In the k-th iteration, the candidate monitoring section that minimizes the aggregation error is selected, that is,

$$x_k^* = \arg\min_{x \in \mathcal{V} \setminus S_{k-1}} J(S_{k-1} \cup \{x\}) \tag{17}$$

Accordingly, the monitoring section set is updated as:

$$S_k = S_{k-1} \cup \{x_k^*\} \tag{18}$$

Repeat the above process until the budget constraint $\mid S_k \mid = N_s$ is satisfied.

For any candidate monitoring cross-section scheme, its evaluation follows a unified closed-loop process, including steps such as reference field construction, virtual sampling, reconstruction solution, error calculation, and training set aggregation.

2.3.3. Computational Complexity and Marginal Benefit of Greedy Search

In each iteration of the forward greedy search, every candidate section in the current candidate set is evaluated by performing a complete reconstruction assessment. Let |V| denote the size of the candidate set and Ns the target number of monitoring sections. The total number of evaluations is as follows:

$$T_{\text{eval}} = \sum_{k=0}^{N_s-1} (|V| - k) = N_s|V| - \frac{N_s(N_s-1)}{2} \tag{19}$$

Denote C_{eval} as the computational cost per evaluation (including reconstruction and error aggregation over the training set). The overall complexity of the greedy algorithm is

$$O(N_s|V| \cdot C_{\text{eval}})$$

In contrast, exhaustive search requires evaluating $\binom{|V|}{N_s}$ combinations. For |V| = 100 and Ns = 12, $\binom{100}{12} \approx 1.05 \times 10^{15}$, which is far larger than $T_{\text{eval}} \approx 100 \times 12 = 1200$ evaluations. Hence, the greedy strategy is computationally feasible.

Define the marginal benefit at the k-th iteration as:

$$\Delta_k = J(S_{k-1}) - J(S_k) \tag{20}$$

From Equation (13), $J(S)$ is non-increasing as more sections are added, so $\Delta_k \geq 0$. Numerical results show that Δ_k typically decreases with increasing k, i.e., the following diminishing-returns property is empirically observed:

$$\Delta_{k+1} \leq \Delta_k \tag{21}$$

This property, known as submodularity, is commonly exploited in sensor placement problems to justify the use of greedy algorithms [31,32]. While a rigorous proof of submodularity for the specific set function $J(S)$ is mathematically nontrivial, the empirical evidence and validation against the exhaustive enumeration for smaller budgets strongly support the near-optimality of the greedy solution. For a monotone submodular function, the solution S_k obtained by the greedy algorithm satisfies:

$$J(S_k) \leq \left(1 - e^{-k/N_s}\right) J(S_{\text{opt}}) \tag{22}$$

where S_{opt} is the theoretical optimal set. This bound provides an approximation guarantee, and our numerical experiments confirm that the greedy-selected layouts perform very close to the optimum.

To further reduce computational cost, a stopping threshold $\varepsilon > 0$ can be introduced. If $\Delta_k < \varepsilon$ at an iteration, the subsequent marginal benefits will be even smaller, and the iteration can be terminated early with S_k as the final scheme. In this work, $\varepsilon = 10^{-4}$ is adopted. For all budget levels considered (N_s), early termination is never triggered, indicating that the marginal benefit remains significant within the given budget range.

3. Numerical Model and Simulation Setup

This chapter describes the numerical simulation setup used to build a verification benchmark for the reconstruction algorithm. High-precision reference field data is obtained through finite element analysis (FEA), and the optimal monitoring section scheme corresponding to different reconstruction algorithms is given through a greedy search strategy, providing a unified numerical benchmark for subsequent virtual sampling, monitoring section optimization, and reconstruction performance evaluation.

3.1. Structural Configuration and Boundary Conditions

In order to establish a numerical verification benchmark for the reconstruction algorithm, this paper uses COMSOL Multiphysics® v. 6.1 to build a three-dimensional suspended pipeline model. The research object is a thin-walled cylindrical shell structure, and its geometric dimensions are scaled according to a 1:10 ratio based on a pipe with an outer diameter of 762 mm (30 in) in the engineering prototype. The total length of the model is L = 3000 mm, the outer radius is R = 38 mm, and the wall thickness is t = 2 mm. In order to facilitate the parametric expression of the surface field, (x, θ) is used to describe the outer surface position of the pipeline, where the axial coordinate is $x \epsilon$ [−1500, 1500] mm and the circumferential angle is $\theta \ \epsilon \ [0, 2\pi]$. In terms of material parameters, the pipeline material is assumed to be isotropic linear elastic steel (API X60), with elastic modulus $E = 2.1 \times 10^5$ MPa and Poisson's ratio $\nu = 0.3$. A summary of the geometric and material parameters is shown in Table 1.

Table 1. Numerical simulation of physical parameters.

Category	Description	Symbol	Value	Unit
Geometry	Total pipe length	L	3000	mm
	Outer radius	R	38	mm
Material	Elastic modulus	E	2.1×10^5	MPa
	Poisson's ratio	N	0.3	-
Coordinate	Axial range	X	[−1500, 1500]	mm
	Angle range	Θ	$[0, 2\pi]$	rad

The corresponding coordinate definitions and boundary conditions are shown in Figure 4. The left end of the pipe $x = -L/2$ is set as fixed-support end A, which is used to constrain the rigid body movement of the end; the right end $x = L/2$ is set as rolling-hinge-support end B, which provides lateral support while allowing for axial free expansion and contraction, that is, the axial displacement of the release end B u_x. This boundary condition corresponds to the simplified support form of "fixed support–rolling support", which can avoid the overall rigid body drift of the structure and allow for the axial expansion and contraction of the pipe section [33].

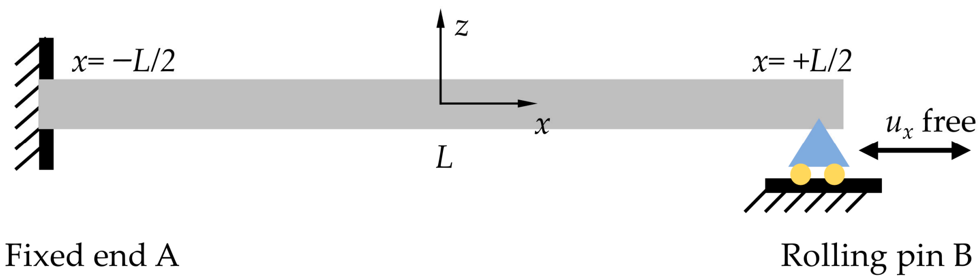

Figure 4. Geometric parameters, coordinate system, and boundary conditions of the pipe model.

The numerical solution was completed on the COMSOL Multiphysics platform, and the model was discretized using eight-node hexahedral linear elements. The meshing results are shown in Figure 5.

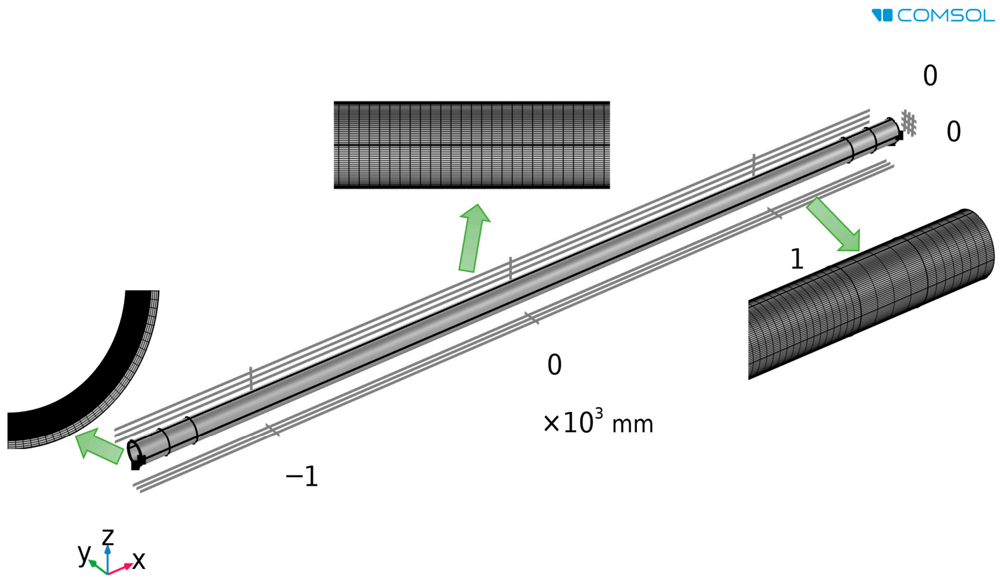

Figure 5. High-fidelity finite element mesh for numerical simulation.

To verify mesh independence, a systematic convergence study was performed using four mesh levels (coarse, medium, fine, and extra-fine) under a representative Type A load ($f_0 = 3000$ N, $x_c = 0$ mm, $\sigma_{xA} = 1200$ mm, $\phi = 0°$). Table 2 summarizes the mesh characteristics and corresponding maximum von Mises stress and maximum displacement. After mesh convergence analysis, the final model contains 33,600 elements and 42,600 nodes.

Table 2. Mesh independence test for the finite element pipeline model.

Mesh Level	No. of Elements	No. of Nodes	Max. Von Mises Stress (MPa)	Max. Displacement (mm)	Relative Change in Stress (%)
Coarse	12,800	16,800	78.2	3.81	–
Medium	22,400	28,600	81.0	3.90	3.6
Fine	33,600	42,600	81.9	3.92	1.1
Extra-fine	48,200	61,800	82.1	3.93	0.2

Note: Fine mesh was adopted in this study. The relative change from fine to extra-fine is 0.2%, indicating mesh independence.

3.2. Load Case Design and Data Set Construction

Based on the COMSOL parametric scanning results, this article constructed a finite element benchmark library containing 60 groups of static working conditions. The working condition library covers three representative scenarios (A/B/C) of axial distributed load, local load and composite load, and is used to provide high-precision reference solutions for the unified comparative evaluation of subsequent reconstruction algorithms.

3.2.1. Load Category and Distribution

In the finite element model, the external load is applied to the outer surface boundary of the pipe in the form of surface force per unit area. The spatial distribution of the load is expressed as a function of axial coordinate x and circumferential angle θ:

$$\mathbf{t}(x,\theta) = \frac{f_0}{Q} \cdot h(x,\theta) \cdot \mathbf{n}(\phi), \tag{23}$$

$\mathrm{t}(x,\theta)$ is the traction vector (force per unit area) applied to the pipe's outer surface; f_0 is the reference resultant force amplitude (with unit of force); $h(x, \theta) \epsilon$ [0, 1] is a dimensionless spatial window function that describes the normalized load distribution along the axial and circumferential directions; and $\mathbf{n}(\phi)$ is the unit vector specifying the load direction, with ϕ being the angle of the load direction relative to the pipe axis. Q is a normalization factor introduced to ensure that the total resultant force is independent of the load window size, defined as:

$$Q = \int_0^{2\pi} \int_{-L/2}^{L/2} h(x,\theta) R dx d\theta, \tag{24}$$

with R being the pipe radius and L the pipe length.

Subsequently, the load amplitude is normalized to ensure that different working conditions have a consistent basis for comparison in terms of equivalent total load magnitude, thereby eliminating the impact of differences in load action area on the reconstruction performance evaluation.

3.2.2. Load Type Definition

To simulate the main threats encountered by subsea suspended pipelines in actual marine environments, and to capture the corresponding engineering stress characteristics across different scales, this paper constructs three representative load window functions (categories A, B, and C), as shown in Figure 6.

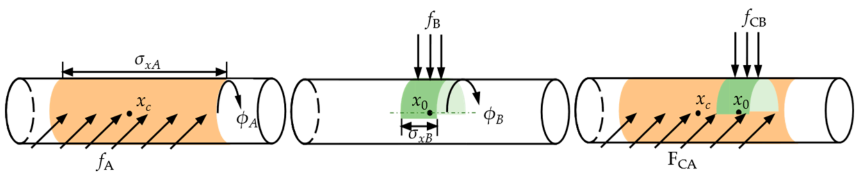

Figure 6. Schematic illustration of the representative loading cases applied to the pipeline: (**a**) axial distributed load (Case A); (**b**) localized vertical load (Case B); (**c**) combined loading condition (Case C).

Category A (axial distributed load) corresponds to the bending moment and axial stress distribution induced by wave/current actions on the free-spanning section [34]. This load covers a certain suspended span along the axial direction and adopts a unimodal Gaussian distribution form:

$$h_A(x) = \exp[-(x-x_c)^2/(2\sigma_{xA}^2)], \tag{25}$$

x_c is the axial center position and σ_{xA} represents the axial action width.

Category B (local extrusion load) simulates accidental events such as dropped anchors or falling objects that cause local dents and high stress concentrations in subsea pipelines [35]. These loads are locally distributed in both the axial and circumferential directions to simulate stress situations such as local extrusion:

$$h_B(x,\theta) = h_{xB}(x)h_\theta(\theta), \;\; h_{xB}(x) = \exp\left(-\frac{(x-x_0)^2}{2\sigma_{xB}^2}\right), \tag{26}$$

Among them, the circumferential window function takes a periodic form to satisfy the circumferential continuity in the θ direction, for example,

$$h_\theta(\theta) = \exp\left(-\frac{\mathrm{wrap}_{[-\pi,\pi]}(\theta-\theta_0)^2}{2\sigma_\theta^2}\right) \tag{27}$$

Type C (combined load) constructs an asymmetric, multi-scale stress state through the superposition of Class A and Class B loads, reflecting the multi-axial stress condition when a dented pipeline is further subjected to global bending, axial force, and external hydrostatic pressure [36]. It is used to test the global restoration ability of the reconstruction algorithm under complex distributions. Its window function can be expressed as:

$$h_C(x,\theta) = \eta h_A(x) + (1-\eta)h_B(x,\theta), \;\; \eta \in [0,1]. \tag{28}$$

η is the combined weight of the load window functions of Class A and Class B, and is unified and normalized according to Equations (23) and (24).

3.3. Parameter Setup and iFEM Algorithm Calibration

3.3.1. Load Parameter Setup

Twenty groups of working conditions were generated for the three types of loads A/B/C, totaling 60 groups, and automated static solution was performed to obtain the full-field displacement and strain response as benchmark data. A summary of load parameterization variables and value rules is shown in Table 3. In order to ensure that parameter calibration and performance evaluation are independent of each other, this article divides the working conditions into a calibration set and an independent test set.

Table 3. Summary of load parameterization definition and variation rules.

Parameter	Symbol	Variation Range/Rule	Value
Combined Effort	f_0	3000	N
Direction Angle	ϕ	{0°, 90°, 180°, 270°}	deg
Axial Center (Class A/C)	x_c	[−1200, 1200]	mm
Axial Center (Class B)	x_0	[−1200, 1200]	mm
Characteristic Width (Class A/C)	σ_{xA}	{600, 1200, 1800}	mm
Characteristic Width (Class B)	σ_{xB}	100	mm

3.3.2. iFEM Algorithm Parameter Calibration

Based on the 60 sets of numerical operating conditions constructed in Section 3.2, this paper further carries out iFEM parameter calibration. For the three types of loads A, B, and C, 20 groups of working conditions are generated for each type, totaling 60 groups,

The full-field displacement and strain response are obtained through automated static solution as benchmark data. In order to ensure that parameter calibration and performance evaluation are independent of each other, the dataset is divided using a stratified sampling method by load type. Specifically, from the 24 Type A cases, 18 Type B cases, and 18 Type C cases, 8, 6, and 6 cases are respectively selected to form a test set of 20 cases (test20), while the remaining 40 cases constitute the calibration set (train40). The calibration set is used for iFEM parameter calibration, as shown in Table 4. The further optimization of monitoring cross-sections is carried out after the calibration parameters are fixed. The test set is used to carry out a strict and independent reconstruction performance evaluation.

Table 4. Optimized parameters and hyperparameters for the iFEM (iQS4) framework.

Category	Parameter	Symbol	Value
Data fidelity	Axial strain residual weight	w_x	3.0
Data fidelity	Circumferential strain residual weight	w_θ	0.1
Smoothing	Smoothing regularization coefficient for transverse displacement	λ_s	100
Stability	Tikhonov regularization coefficient	λ_{Tik}	10^{-6}
Boundary	Boundary penalty coefficient	β	10^8

The hyperparameters listed in Table 4 were determined through systematic sensitivity analysis on the train40 calibration set (40 working conditions). For data fidelity, the axial strain weight $w_x = 3.0$ is larger than the circumferential weight $w_\theta = 0.1$ because axial strain dominates the pipeline response under bending loads; this ratio minimized the reconstruction error $\mathrm{NRMSE}_{\mathrm{combo}}$ over the calibration set. The smoothing coefficient $\lambda_s = 100$ was selected after a grid search over [100, 104]; values below 10^1 led to visible displacement oscillations under sparse monitoring, while values above 10^3 over smoothed local deformation features. The Tikhonov coefficient $\lambda_{Tik} = 10^{-6}$ is the smallest value that ensures a well-conditioned system matrix (condition number < 10^9) for all training cases. The boundary penalty coefficient $\beta = 10^8$ follows common practice in penalty methods for essential boundary conditions, enforcing constraints within machine precision without causing ill conditioning. All parameters were fixed before monitoring section optimization and the independent testing on the test20 set; their robustness is demonstrated by the stable reconstruction errors across different budget levels shown in Section 4.4.

4. Numerical Results and Discussion

4.1. Evaluation System and Error Indicators

It should be noted that the search objective function defined in Section 2.3 is only used for screening candidate monitoring sections in the greedy search stage and is not used as a unified evaluation criterion for the final reconstruction performance. The monitoring point set P used in this chapter follows the optimal monitoring cross-section scheme determined in Section 3.3. The virtual monitoring strain $\varepsilon^{\mathrm{obs}}$ is obtained by sampling the numerical datum field at the corresponding monitoring position, and is used as a unified input for the iFME reconstruction methods [37].

After the point layout plan is determined and the reconstruction calculation is completed, to objectively evaluate the final reconstruction quality, this paper adopts a regular sampling strategy in the parameter domain. Specifically, N_x = 81 points are uniformly taken in the axial direction (over the length L = 3000 mm), and N_θ = 72 points are uniformly taken along the circumferential direction (every 5° over 0° to 360°), yielding a total of $N_x \times N_\theta = 81 \times 72 = 5832$ evaluation points. Based on these sampling points, a result evaluation index system is formed using the normalized root mean square error (NRMSE) and the peak relative error ($\mathrm{REP}_{\mathrm{peak}}$). Differing from the search objective function in Section 2.3.3, the indicators in this section are used in the post hoc inspection and method comparison of the final reconstruction results [38].

Suppose there are N evaluation nodes in total on the regular sampling grid, the reference value at the i-th node is $\varepsilon^{\text{ref}}(x_i, \theta_i)$, and the reconstructed value is $\hat{\varepsilon}(x_i, \theta_i)$; then, the NRMSE of this component is defined as:

$$NRMSE = \frac{\sqrt{\frac{1}{N}\sum_{i=1}^{N}\left(\hat{\varepsilon}(x_i, \theta_i) - \varepsilon^{\text{ref}}\,(x_i, \theta_i)\right)^2}}{\max\left(\varepsilon^{\text{ref}}\right) - \min\left(\varepsilon^{\text{ref}}\right)} \tag{29}$$

Considering that the pipe surface strain field contains two components, axial strain and circumferential strain, this paper calculates NRMSE_x and NRMSE_θ, respectively, and further defines comprehensive indicators:

$$NRMSE_{combo} = \sqrt{\frac{1}{2}(NRMSE_x^2 + NRMSE_\theta^2)}, \tag{30}$$

This index is used to measure the overall error level when two types of strain components are reconstructed simultaneously.

It may be difficult to fully reflect the recovery quality of local extreme regions using only the full-field mean square error. In order to supplement the evaluation of peak identification ability, this article further introduces the relative error of peak (REP_{peak}). Assume that the reference peak and reconstructed peak are $\varepsilon_{\text{peak}}$ and $\hat{\varepsilon}_{\text{peak}}$, respectively; then,

$$REP_{peak} = \frac{\left|\hat{\varepsilon}_{\text{peak}} - \varepsilon_{\text{peak}}\right|}{\left|\varepsilon_{\text{peak}}\right|} \times 100\%, \tag{31}$$

$\varepsilon_{\text{peak}}$ and $\hat{\varepsilon}_{\text{peak}}$ are the reference peak and reconstructed peak, respectively. Therefore, this paper uses a two-layer index system of "full-field error + peak error" to conduct a unified evaluation of the reconstruction results under different conditions.

4.2. Optimal Monitoring Cross-Section Layout

Based on the greedy search strategy proposed in Section 2.3, this paper further determines the optimal monitoring cross-section layouts corresponding to the iFEM reconstruction algorithm under different levels of monitoring resource allocation. The number of monitoring sections is divided into four levels: B05, B07, B09 and B12. Since this article uses the axial monitoring section as the point distribution unit, and each section is configured with four fixed circumferential measuring points, the four budget levels correspond to N_s = 5, 7, 9, and 12 monitoring sections, respectively, and the total number of monitoring points is N_p = 20, 28, 36, and 48, respectively.

Table 5 lists the optimal layout schemes of iFEM for different numbers of monitoring sections, while Figure 7 shows the corresponding spatial distribution. As the number of monitoring sections increases, the iFEM-optimized layouts obtained by the greedy search exhibit a general trend of prioritizing coverage of key areas and gradually expanding to the entire analysis domain.

Table 5. Monitoring Point Layout Plan and Parameter Configuration.

Scheme	Total Points (N_p)	Axial Coordinates x (mm)
B05_{iFEM}	20	−1350, 900, 1100, 1200, 1350
B07_{iFEM}	28	−1350, −1150, 700, 900, 1100, 1200, 1350
B09_{iFEM}	36	−1350, −1250, −1150, −1000, 700, 900, 1100, 1200, 1350
B12_{iFEM}	48	−1350, −1250, −1150, −1000, −250, 500, 700, 800, 900, 1100, 1200, 1350

https://doi.org/10.3390/infrastructures11050160

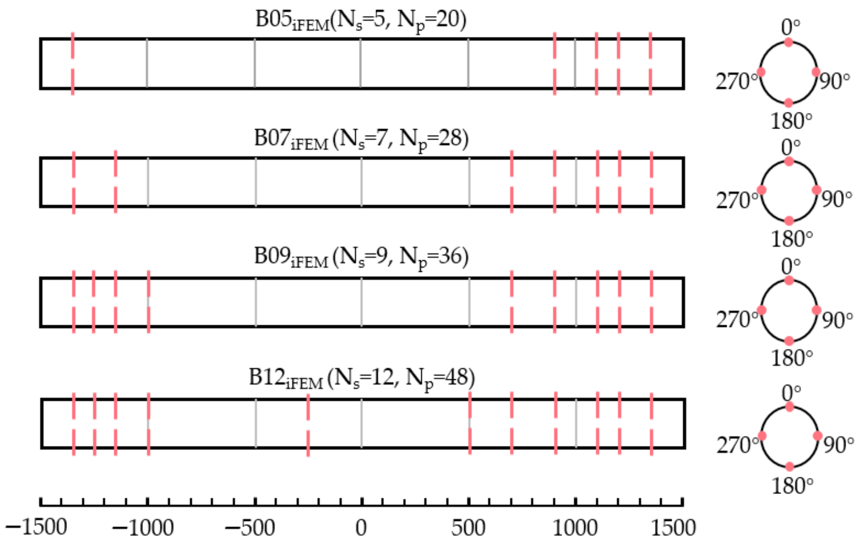

Figure 7. Optimal sensor layout and monitoring point quantities under iFEM reconstruction methods.

Specifically, at lower budget levels (B05, B07), iFEM tends to prioritize sections near the pipe's end boundaries and constraint-related areas; as the budget increases to B09 and B12, the selected sections gradually expand towards the mid-span area, while still maintaining effective coverage of the boundary areas. This distribution pattern confirms that the greedy search strategy yields optimal iFEM-specific monitoring layouts, which exhibit a strong dependence on boundary information and significant spatial localization rather than uniform distribution.

4.3. Comparison of Axial Strain Fields Under Typical Conditions

In order to intuitively compare the reconstruction capabilities of different reconstruction methods on the axial strain field and peak characteristics under sparse monitoring conditions, this section selects the representative working case B09-case045 from the test set. Figure 8 shows a comparison between the numerical reference field and the reconstruction results of the interpolation method and iFEM.

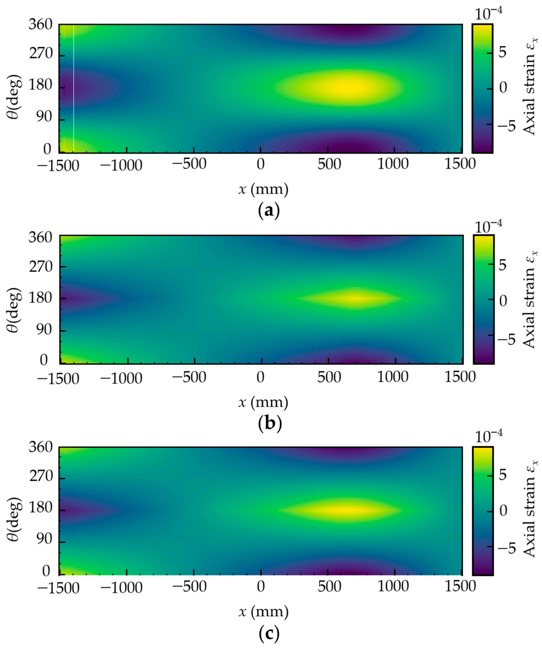

Figure 8. Comparison of axial strain field distributions in the (x, θ) domain: (**a**) finite element (FE) reference solution; (**b**) interpolation-based reconstruction; (**c**) iFEM-based reconstruction.

As shown in Figure 8a, the numerical reference field forms a continuous positive strain peak area in the middle–right area of the pipe section, and its circumferential center is roughly located near $\theta = \pi$.

As can be seen from Figure 8b, the interpolation method can identify the approximate position of the main peak area, but there is obvious geometric distortion in the shape of the peak area. The specific manifestation is that the high-value area is elongated along the axial direction, shrinks along the circumferential direction, and presents a narrow strip distribution, resulting in the width of the peak area being inconsistent with the numerical reference field. At the same time, the transition area is compressed, indicating that this method still shows a certain deviation in the recovery of local high-gradient areas.

In contrast, the iFEM reconstruction result shown in Figure 8c is also able to identify the center position of the peak area and is closer to the reference field in terms of spatial envelope and gradient transition. Compared with the interpolation method, iFEM suppresses the abnormal shrinkage of high-value areas to a certain extent, making the axial width and overall shape of the peak area more consistent with the reference distribution, and thus showing better morphological consistency and stability.

Therefore, we will focus on analyzing the reconstruction accuracy of the iFEM method under different layout schemes.

4.4. Accuracy Analysis Under Various Layout Schemes

After completing a comparative analysis of typical working conditions, this section further extends the evaluation scope to the complete test set, and systematically compares the reconstruction error distributions of the iFEM under four point layout budgets (B05, B07, B09, B12). Statistical indicators include $\mathrm{NRMSE}_{\mathrm{combo}}$, $\mathrm{REP}_{\mathrm{peak}}$, NRMSE_x and NRMSE_θ, as shown in Figure 9. To reduce the influence of single-case outliers, box plots are used to display the error distribution, with the median representing the typical error level; the error trend is analyzed together with the number of monitoring sections N_s. In each box plot, the box boundaries denote the lower and upper quartiles (interquartile range, IQR), the whiskers extend to the most extreme data points within 1.5 × IQR, and points beyond the whiskers are considered outliers.

Based on the optimal monitoring section scheme obtained by the greedy algorithm, the following characteristics are observed from the analysis of $\mathrm{NRMSE}_{\mathrm{combo}}$, $\mathrm{REP}_{\mathrm{peak}}$, NRMSE_x and NRMSE_θobtained by iFEM reconstruction:

(1) Regarding overall accuracy and diminishing marginal returns, the average $\mathrm{NRMSE}_{\mathrm{combo}}$ lies between 0.030 and 0.035 across all budget levels (as shown in Figure 9a). As N_s increases, the error decreases, with the most significant reduction occurring when raising the budget from B05 ($N_s = 5$) to B07 ($N_s = 7$). Further increases to B09 and B12 yield only marginal gains, and the box-plot interquartile ranges (IQRs) of B07, B09 and B12 overlap substantially, with medians remaining nearly constant, indicating that the error difference beyond $N_s \geq 7$ is not significant. The median trend line connected across budgets confirms a steep drop from B05 to B07 followed by a plateau.

(2) Concerning peak strain reconstruction accuracy and stability, Figure 9b presents the boxplot distribution of $\mathrm{REP}_{\mathrm{peak}}$ under different monitoring budgets. The overall mean $\mathrm{REP}_{\mathrm{peak}}$ of iFEM is relatively large (typical value below 0.4). For $N_s = 5$, the $\mathrm{REP}_{\mathrm{peak}}$ ranges from 0.1 to 0.9, indicating considerable dispersion. When $N_s \geq 7$, the IQR becomes much shorter, the dispersion decreases significantly, and the data concentrate around the median, showing that model stability improves and $\mathrm{REP}_{\mathrm{peak}}$ becomes insensitive to further budget increases.

(3) In terms of axial strain reconstruction (Figure 9c,d), the average $NRMSE_x$ ranges from 0.010 to 0.020, while the average $NRMSE_\theta$lies between 0.040 and 0.050. The axial strain error is significantly lower than the circumferential error.

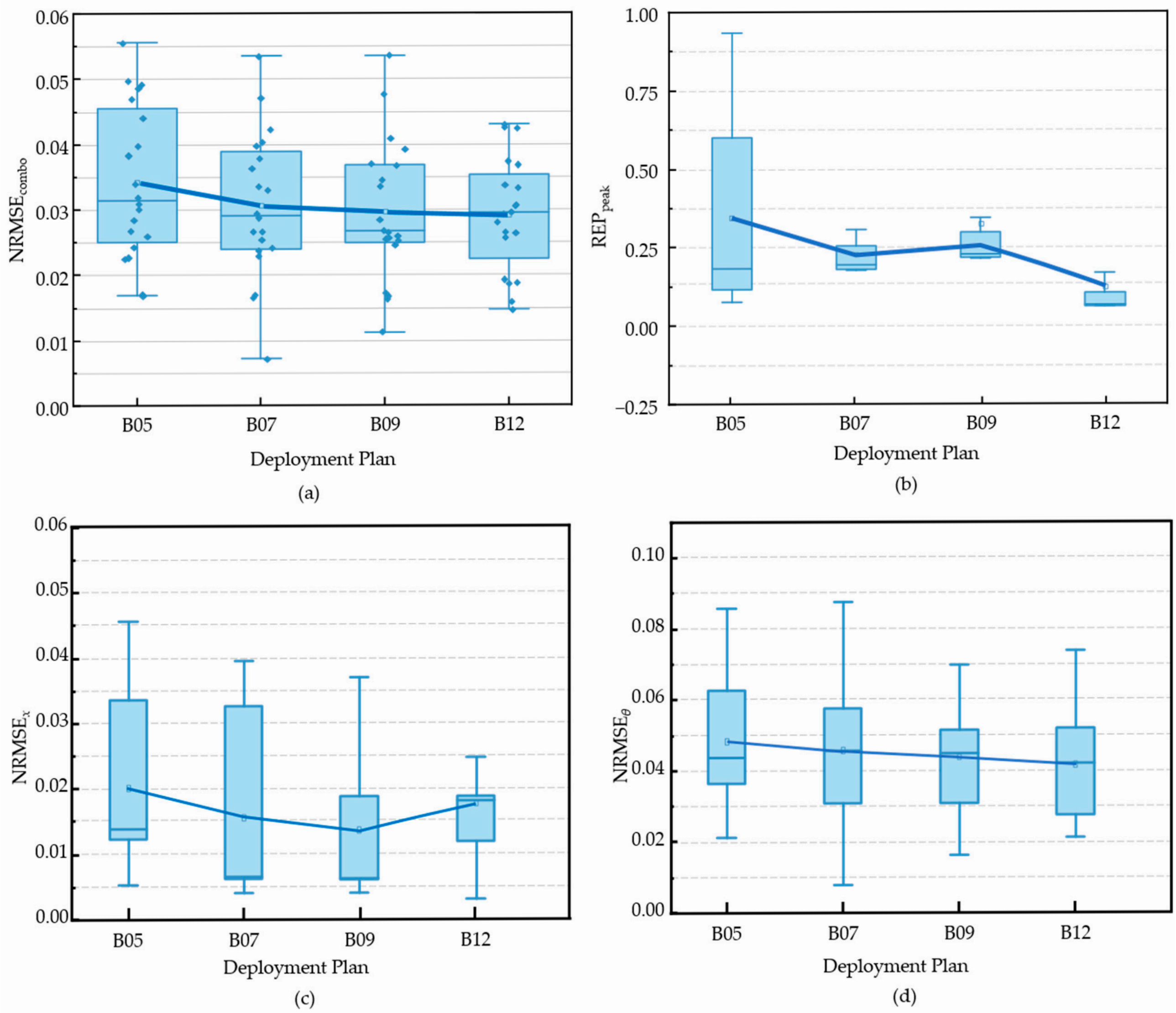

Figure 9. Full-field composite reconstruction error distribution under different monitoring budgets: (**a**) $NRMSE_{combo}$; (**b**) REP_{peak}; (**c**) axial strain error $NRMSE_x$; (**d**) circumferential strain error $NRMSE_{\theta.}$

In summary, the greedy-optimized iFEM framework achieves high-accuracy full-field strain reconstruction even under sparse budgets (e.g., B05). No outliers (points beyond 1.5 × IQR) are observed in any of the box plots, confirming the numerical robustness of the iFEM reconstruction. Although the peak relative error is relatively large at very low budgets (B05), it stabilizes quickly once $N_s \geq 7$. Axial strain reconstruction is markedly superior to circumferential strain reconstruction. The method is well-suited for monitoring subsea suspended pipelines where axial loads dominate.

4.5. Discussion

The optimal monitoring-section layouts obtained via the greedy algorithm (Table 5) reveal that iFEM prioritizes boundary and constraint regions under low budgets (B05, B07) and progressively expands toward the mid-span as the budget increases. This boundary-dependent behavior is consistent with previous iFEM studies on pipelines, demonstrating that different sensor layouts can lead to substantially different reconstruction accuracies [26].

Such sensitivity underscores the necessity of optimizing the spatial configuration of monitoring sections for iFEM-based reconstruction.

The reconstruction accuracy exhibits a clear pattern of diminishing marginal returns. The most substantial error reduction occurs when the budget increases from B05 to B07, whereas further increments to B09 and B12 yield only marginal gains. From an engineering perspective, deploying more than nine monitoring sections (B09) provides negligible improvement; thus, the budget range B07–B09 represents the optimal trade-off between reconstruction fidelity and deployment cost. This pattern aligns with the submodularity principle commonly encountered in sensor placement problems, wherein each additional sensor contributes less to performance enhancement than its predecessor, and a greedy algorithm is known to be near-optimal for monotone submodular objective functions [32]. Although a formal proof of submodularity for the specific set function $J(S)$ remains beyond the scope of the present work, the empirically observed diminishing returns provide a practical justification for the adopted greedy search strategy.

The axial strain error is significantly lower than the circumferential error, a finding attributable to the dominant bending load pattern in the considered scenarios, where the pipeline response is primarily governed by axial strains. A similar trend has been documented in recent iFEM studies [24], suggesting that when monitoring resources are limited, prioritizing axial strain measurements can enhance overall reconstruction fidelity—a practical guideline for the field deployment of sparse sensor networks.

Compared to GA- or PSO-based sensor placement methods [27,28], the proposed greedy optimization framework offers a distinct computational advantage: it eliminates the need for algorithm-specific parameter tuning (e.g., population size in GA, inertia weight in PSO) and sequentially selects monitoring sections based solely on the marginal benefit $\Delta_k = J(S_{k-1}) - J(S_k)$. The empirically observed submodularity of $J(S)$ naturally justifies the greedy strategy, which is known to be near-optimal for monotone submodular functions [32]. Consequently, the proposed framework is deterministic, reproducible, and well-suited for engineering applications that demand transparency and simplicity.

5. Conclusions

This paper addresses the problem of sparse strain monitoring for subsea suspended pipelines by proposing a greedy search strategy to obtain the optimal monitoring cross-sections. This approach not only greatly improves computational efficiency but also enhances the reconstruction accuracy of the iFEM strain field. The results show that iFEM tends to prioritize coverage of boundary- and constraint-related regions when selecting monitoring sections.

Under the greedy-optimized iFEM framework, the reconstruction accuracy at different budget levels is quantitatively characterized as follows: the average comprehensive error $\mathrm{NRMSE}_{\mathrm{combo}}$ lies between 0.030 and 0.035 for all budgets. The average axial strain error NRMSE_x is significantly lower than the average circumferential strain error NRMSE_θ. In terms of peak strain reconstruction, the peak relative error ($\mathrm{REP}_{\mathrm{peak}}$) stabilizes quickly once the number of monitoring sections reaches seven (B07). Overall, as the number of monitoring sections increases from B05 to B12, the improvement in reconstruction accuracy exhibits a clear diminishing-return trend: the most significant gain occurs when increasing from B05 to B07, while further increases to B09 and B12 bring only marginal benefits. Under the model and case library considered in this paper, the budget range B07–B09 represents a favorable balance between reconstruction accuracy and deployment cost.

Therefore, the proposed greedy-optimized iFEM framework provides a computable and reproducible implementation for full-field strain reconstruction under sparse strain monitoring conditions for subsea suspended pipelines, and offers a generalizable analytical framework for monitoring layout design under constraints on the number of monitoring sections. However, numerical simulations do not account for real ocean environmental complexities (e.g., random wave loading, soil–pipe interaction) and the reconstruction accuracy may be lower for pre-existing local buckling in pipelines. The framework can be extended to other cylindrical shells (e.g., risers, cables) by regenerating the training case library and recalibrating the hyperparameters.

In practical engineering applications, further consideration is needed for uncertain factors such as the long-term stability of fiber optic sensors in seawater, coupling efficiency, and data acquisition reliability, as well as the sensitivity and robustness of iFEM parameter selection and reconstruction results to external disturbances. In the future, we will perform engineering verification using sensor monitoring data from actual sea trials or experimental tests, and systematically compare other optimization algorithms (e.g., GA, PSO) and reconstruction methods (e.g., interpolation) to develop a hybrid optimization framework for improved monitoring layout design.

Author Contributions: Conceptualization, X.R. and J.C.; methodology, X.R.; validation, X.R. and S.S.; formal analysis, J.Z. and Z.Z.; writing—original draft preparation, X.R. and Y.L. All authors have read and agreed to the published version of the manuscript.

Funding: This research was funded by the Key Research and Development Program of Zhejiang Province (No. 2024SSYS0089) and the Program of Marine Economy Development Special Fund (Six Marine Industries) under Department of Natural Resources of Guangdong Province (Project No. GDNRC [2024]34).

Institutional Review Board Statement: Not applicable.

Informed Consent Statement: Informed consent was obtained from all subjects involved in the study.

Data Availability Statement: Relevant research data are mostly displayed in the paper. If you need other data, you can contact the author by email (except private data).

Acknowledgments: Thanks to all the participants in the research content of this paper.

Conflicts of Interest: The authors declare no conflicts of interest.

Abbreviations

The following abbreviations are used in this manuscript:

iFEM	Inverse Finite Element Method
SHM	Structural Health Monitoring
GA	Genetic Algorithm
PSO	Particle Swarm Optimization
iQS4	Inverse Shell Element
FEA	Finite Element Analysis
NRMSE	Normalized Root Mean Square Error
REPpeak	Relative Error of Peak

References

1. *DNV-OS-F101*; Submarine Pipeline Systems. DNV: Høvik, Norway, 2013.
2. Zhang, B.; Gong, R.; Wang, T.; Wang, Z. Causes and Treatment Measures of Submarine Pipeline Free-Spanning. *J. Mar. Sci. Eng.* **2020**, *8*, 329. [CrossRef]
3. Amaechi, C.; Hosie, G.; Reda, A. Review on Subsea Pipeline Integrity Management: An Operator's Perspective. *Energies* **2022**, *16*, 98. [CrossRef]
4. Bai, Y.; Bai, Q. *Subsea Pipelines and Risers*; Elsevier: Amsterdam, The Netherlands, 2005.
5. Ho, M.; El-Borgi, S.; Patil, D.; Song, G. Inspection and monitoring systems subsea pipelines: A review paper. *Struct. Health Monit.* **2020**, *19*, 606–645. [CrossRef]

6. Liu, P.; Yuan, S.; Qiu, L. Development of a PZT-based wireless digital monitor for composite impact monitoring. *Smart Mater. Struct.* **2012**, *21*, 035018. [CrossRef]
7. Pérez-Pérez, E.J.; González-Baldizón, Y.; Fragoso-Mandujano, J.A.; Guzmán-Rabasa, J.A.; Santos-Ruiz, I. Data-Driven Fault Diagnosis in Water Pipelines Based on Neuro-Fuzzy Zonotopic Kalman Filters. *Math. Comput. Appl.* **2024**, *30*, 2. [CrossRef]
8. Pérez-Pérez, E.J.; López-Estrada, F.R.; Valencia-Palomo, G.; Torres, L.; Puig, V.; Mina-Antonio, J.D. Leak diagnosis in pipelines using a combined artificial neural network approach. *Control. Eng. Pract.* **2021**, *107*, 104677. [CrossRef]
9. Liang, X.; Deng, Y.; Wang, Y.; Li, H.; Ma, W.; Wang, K.; Ren, J.; Ma, R.; Zhang, S.; Liu, J.; et al. Intelligent leak monitoring of oil pipeline based on distributed temperature and vibration fiber signals. *Front. Big Data* **2025**, *8*, 1667284. [CrossRef]
10. Lalam, N.; Bukka, S.; Bhatta, H.; Buric, M.; Ohodnicki, P.; Wright, R. Achieving precise multiparameter measurements with distributed optical fiber sensor using wavelength diversity and deep neural networks. *Commun. Eng.* **2024**, *3*, 121. [CrossRef]
11. Chen, S.; Wang, J.; Zhang, C.; Li, M.; Li, N.; Wu, H.; Liu, Y.; Peng, W.; Song, Y. Marine Structural Health Monitoring with Optical Fiber Sensors: A Review. *Sensors* **2023**, *23*, 1877. [CrossRef]
12. Xu, L.; Shi, S.; Huang, Y.; Yan, F.; Wang, X.; Wilson, R.; Zhang, D. Quantification and assessment of steel pitted corrosion using optical frequency domain reflectometry (OFDR)-based distributed fiber optic sensors. *Measurement* **2025**, *256*, 118519. [CrossRef]
13. Xu, C.; Wu, X.; Zhou, Y.; Liang, R.; Cao, C.; Chen, J.; Zheng, X.; Lu, Z.; Wei, C. Health status monitoring of bridge cable and telescopic compensation device based on fiber grating sensing array. *Rev. Sci. Instrum.* **2024**, *95*, 045007. [CrossRef]
14. Sun, S.; Ren, X.; Chen, J.; Zhou, J.; Lin, Y.; Zhou, P. Reconstruction of Three-Dimensional Surface Stress and Strain Fields of Subsea Suspended Pipelines. In *Proceedings of the 2025 2nd International Conference on Intelligent Perception and Pattern Recognition (IPPR), Chongqing, China*; IEEE: Piscataway, NJ, USA, 2025; pp. 67–73. [CrossRef]
15. Zhu, H.; Du, Z.; Tang, Y. Automatic free span assessment for subsea pipelines using static strain data. *Ocean Eng.* **2022**, *263*, 112413. [CrossRef]
16. Li, S.; Coraddu, A.; Brennan, F. A Framework for Optimal Sensor Placement to Support Structural Health Monitoring. *J. Mar. Sci. Eng.* **2022**, *10*, 1819. [CrossRef]
17. Peng, Y.; Ding, L.; Chen, J. Performance evaluation of base-isolated structures with sliding hydromagnetic bearings. *Struct. Control. Health Monit.* **2019**, *26*, e2278. [CrossRef]
18. Ahmed, M.O.; Yenduri, A.; Kurian, V.J. Evaluation of the dynamic responses of truss spar platforms for various mooring configurations with damaged lines. *Ocean Eng.* **2016**, *123*, 411–421. [CrossRef]
19. Wang, J.; Ren, L.; You, R.; Jiang, T.; Jia, Z.; Wang, G.X. Experimental study of pipeline deformation monitoring using the inverse finite element method based on the iBeam3 element. *Measurement* **2021**, *184*, 109881. [CrossRef]
20. Wang, B.; Ke, X.; Du, K.; Bi, X.; Hao, P.; Zhou, C. A novel strain field reconstruction method for test monitoring. *Int. J. Mech. Sci.* **2023**, *243*, 108038. [CrossRef]
21. Dong, Z.; Jia, S.; Shao, C. Filtered kriging for improved interpolation of periodic manufacturing surfaces. *J. Manuf. Process.* **2024**, *131*, 1–12. [CrossRef]
22. Du, J.; Zhao, J.; Liu, J.; Zhao, D. Radial basis point interpolation for strain field calculation in digital image correlation. *Appl. Opt.* **2024**, *63*, 3929. [CrossRef] [PubMed]
23. Wu, M.; Tan, S. Inverse finite element method with energy-based regularization for deformation reconstruction and structural health monitoring. *Thin-Walled Struct.* **2024**, *199*, 111859. [CrossRef]
24. Li, K.; Xiao, L.; Wei, H.; Kou, Y.; Shan, M. A unified framework for enhancing inverse finite element method through strain pre-extrapolation and sensor placement optimization. *Mech. Syst. Signal Process.* **2025**, *234*, 112836. [CrossRef]
25. Gherlone, M.; Cerracchio, P.; Mattone, M.; Di Sciuva, M.; Tessler, A. Shape sensing of 3D frame structures using an inverse Finite Element Method. *Int. J. Solids Struct.* **2012**, *49*, 3100–3112. [CrossRef]
26. Mei, M.; Cheng, H.; Huang, H.; Wu, Z.; Yang, H.; Wu, K. Dynamic analysis and shape sensing of pipes subjected to water hammer by the inverse finite element method. *Measurement* **2025**, *241*, 115701. [CrossRef]
27. Ghasemzadeh, M.; Kefal, A. Sensor Placement Optimization for Shape Sensing of Plates and Shells Using Genetic Algorithm and Inverse Finite Element Method. *Sensors* **2022**, *22*, 9252. [CrossRef] [PubMed]
28. Zhao, Y.; Du, J.; Bao, H.; Xu, Q. Optimal Sensor Placement Based on Eigenvalues Analysis for Sensing Deformation of Wing Frame Using iFEM. *Sensors* **2018**, *18*, 2424. [CrossRef]
29. Tichonov, A.N.; Arsenin, V.J.; Tichonov, A.N. *Solutions of Ill-Posed Problems*; Wiley: New York, NY, USA, 1977.
30. Shimpi, R.P.; Patel, H.G.; Arya, H. New First-Order Shear Deformation Plate Theories. *J. Appl. Mech.* **2007**, *74*, 523–533. [CrossRef]
31. Zheng, L.; Chan, H.; Loukides, G.; Li, M. Maximizing Approximately k-Submodular Functions. In *Proceedings of the 2021 SIAM International Conference on Data Mining (SDM)*; Society for Industrial and Applied Mathematics: Philadelphia, PA, USA, 2021; pp. 414–422. [CrossRef]
32. Liao, W.; Ji, Q.; Wallace, W.A. Approximate nonmyopic sensor selection via submodularity and partitioning. *IEEE Trans. Syst. Man Cybern. Part A Syst. Hum.* **2009**, *39*, 782–794. [CrossRef]
33. Elshafey, A.A.; Haddara, M.R.; Marzouk, H. Free spans monitoring of subsea pipelines. *Ocean Syst. Eng.* **2011**, *1*, 59–72. [CrossRef]

34. Gullaksen, J. Implementation of a Method for Free-Spanning Pipeline Analysis. In *Proceedings of the ASME 2021 40th International Conference on Ocean, Offshore and Arctic Engineering*; American Society of Mechanical Engineers Digital Collection: Livingston, NJ, USA, 2021. [CrossRef]
35. Sun, Q.; Liu, J. Study on the Impact Damage of Submarine Pipelines by Anchor under Emergency Anchorage. *IOP Conf. Ser. Mater. Sci. Eng.* **2018**, *452*, 022078. [CrossRef]
36. Su, W.; Ren, J. Numerical Simulation of Local Buckling of Submarine Pipelines under Combined Loading Conditions. *Materials* **2022**, *15*, 6387. [CrossRef]
37. Chen, G.; Wang, X.; Zhao, N.; Jiang, Z.; Li, F.; Chen, H.; Wei, P.; Zhang, T. Study on Strain Field Reconstruction Method of Long-Span Hull Box Girder Based on iFEM. *J. Mar. Sci. Eng.* **2024**, *12*, 1482. [CrossRef]
38. Mentaschi, L.; Besio, G.; Cassola, F.; Mazzino, A. Problems in RMSE-based wave model validations. *Ocean Model.* **2013**, *72*, 53–58. [CrossRef]

https://doi.org/10.3390/infrastructures11050160